Supplementary Information for:

Engineered spatial inversion symmetry breaking in an oxide heterostructure built from isosymmetric room-temperature magnetically ordered components

J. Alaria[a,b], P. Borisov[a,f], M. S. Dyer[a], T. D. Manning[a], S. Lepadatu[c], M. G. Cain[c], E. D. Mishina[d], N. E. Sherstyuk[d], N.A. Ilyin[d], J. Hadermann[e], D. Lederman[f], J. B. Claridge[a]*, and M. J. Rosseinsky[a]*,.

[a] Department of Chemistry, University of Liverpool, Liverpool, L69 7ZD, UK

[b] Stephenson Institute for Renewable Energy, Department of Physics, University of Liverpool, Liverpool, L69 7ZE, UK

[c] National Physical Laboratory, Hampton Road, Teddington, Middlesex TW11 0LW, UK

[d] Moscow State Technical University of Radioengineering, Electronics and Automation, Vernadsky Avenue 78, 119454 Moscow, Russia

[e] EMAT, University of Antwerp, Groenenborgerlaan 171, B-2020, Antwerp, Belgium.

[f] Department of Physics and Astronomy, West Virginia University, Morgantown, West Virginia, 26506 USA.

1 Calculations of polarisation for heterostructures of different thicknesses

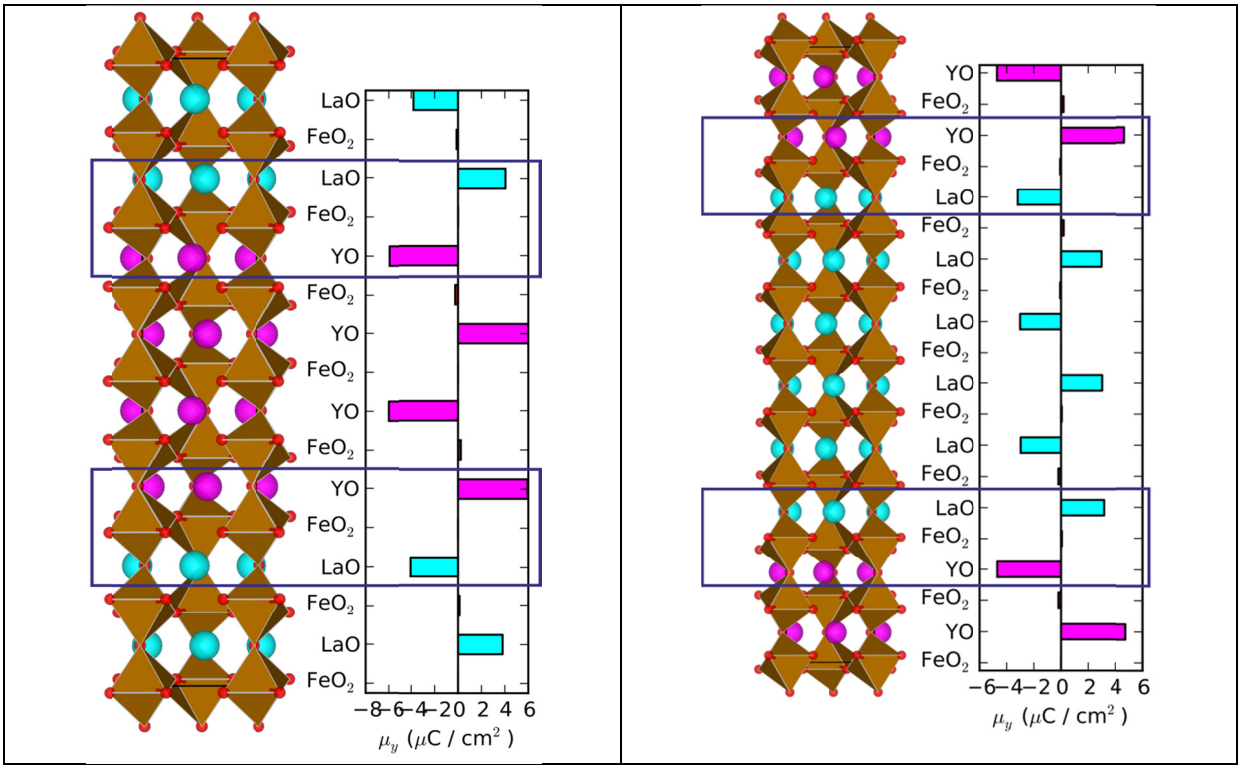

Figure S1. The calculated structure of the $(LaFeO_3)_4(YFeO_3)_4$ (left) and $(LaFeO_3)_6(YFeO_3)_4$ (right) heterostructures are shown alongside the contribution from each layer to the overall polarization. The purple box highlights the interface region where the displacements cancel each other, leading to zero net polarization.

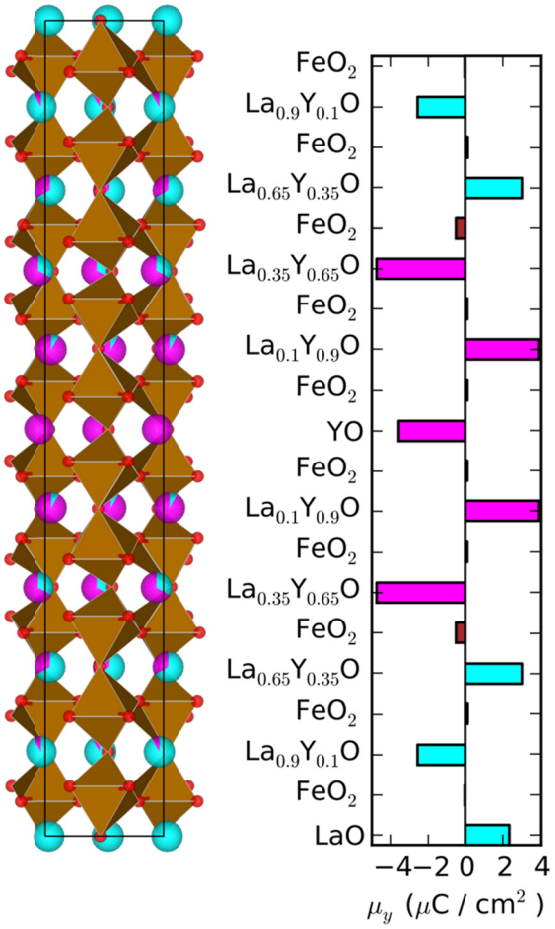

Figure S2. A structural diagram of the model used for the force-field calculation of $(LaFeO_3)_5(YFeO_3)_5$ with sinusoidal variation of the La and Y content along the stacking direction. The occupancy of the sites is represented by pie charts (La cyan, Y purple) on each atomic position. Plotted alongside is the layer-by-layer contribution to the polarisation in the polar direction calculated using static charges.

2 Substrate preparation and structure

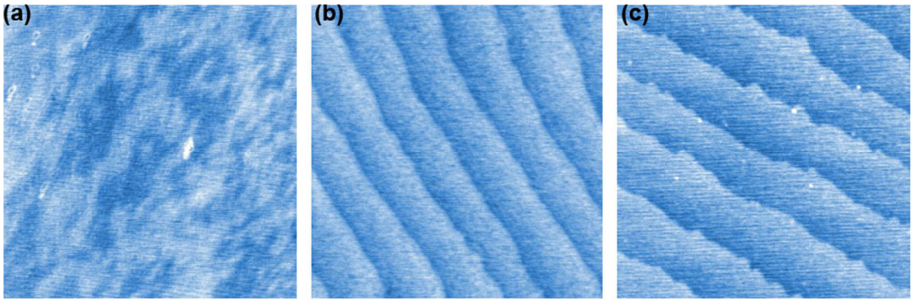

Figure S3. AFM of (a) as received, (b) annealed at 1050^{o}C for 2h in air and (c) etched for 1h in 12M NaOH/DI water solution DSO substrate showing the clear formation of an atomically flat surface

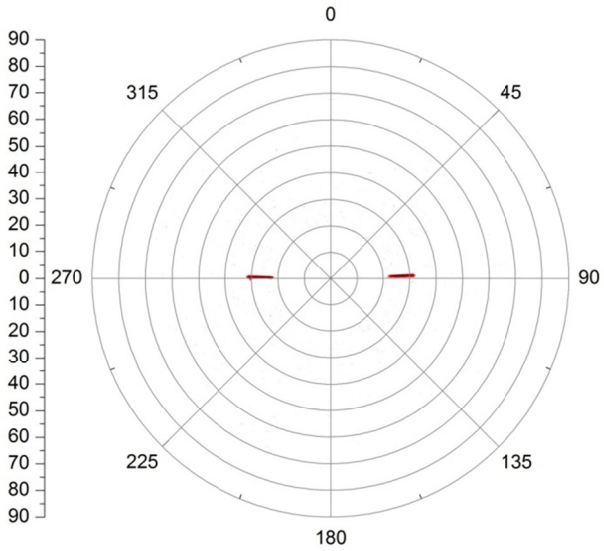

Figure S4. Pole figure on the $(111)_{Pnma}$ reflection of the DSO substrate showing a twofold symmetry, indicative of the two domains with the b_{Pnma} in plane.

3 Thin film growth

We observed layer-by-layer growth for $LaFeO_3$ on $SrTiO_3$ [100] (STO) above 600 ºC (Supplementary Figure S4); below 600 ºC surface mobility is insufficient to induce crystallinity in the growing layers.

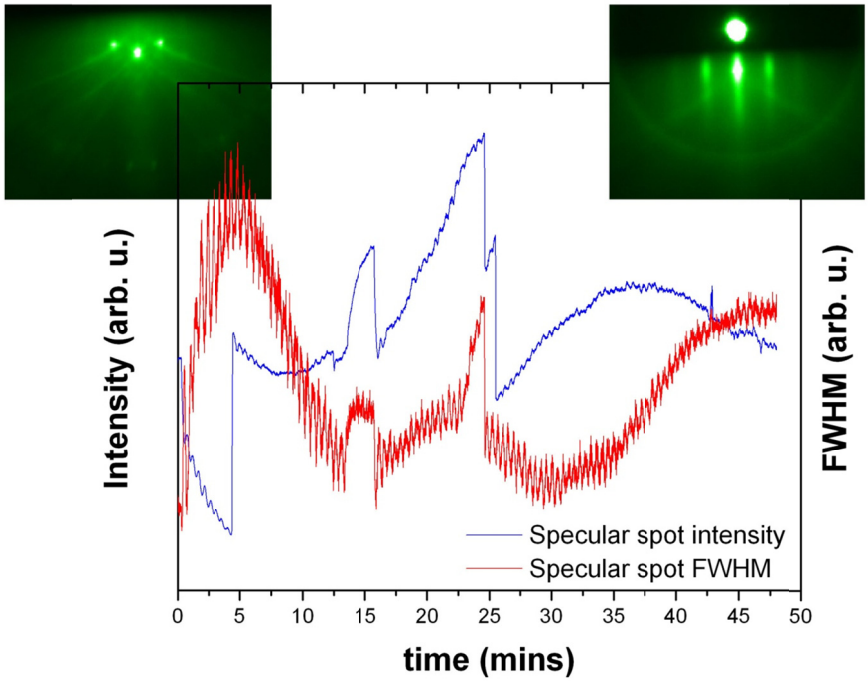

Figure S5. RHEED study of $LaFeO_3$ deposited in the same experimental conditions of the main text, showing sustained oscillation in both the specular intensity and FWHM of the specular spot

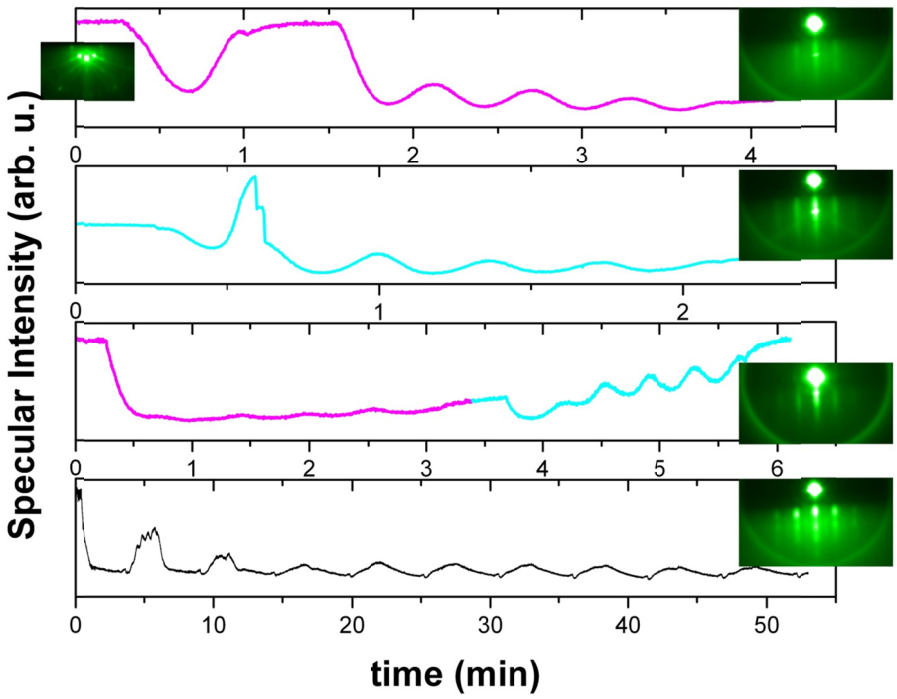

Figure S6. RHEED study of a $(LaFeO_3)_5(YFeO_3)_5$ heterostructure on STO showing the difficulty of obtaining clear RHEED oscillation for the YFO layer after a few monolayer. The RHEED pattern remains streaky indicating a 2 dimensional growth throughout the structure. The colour coding is identical to that in the main text (magenta for $YFeO_3$ and cyan for $LaFeO_3$ layer)

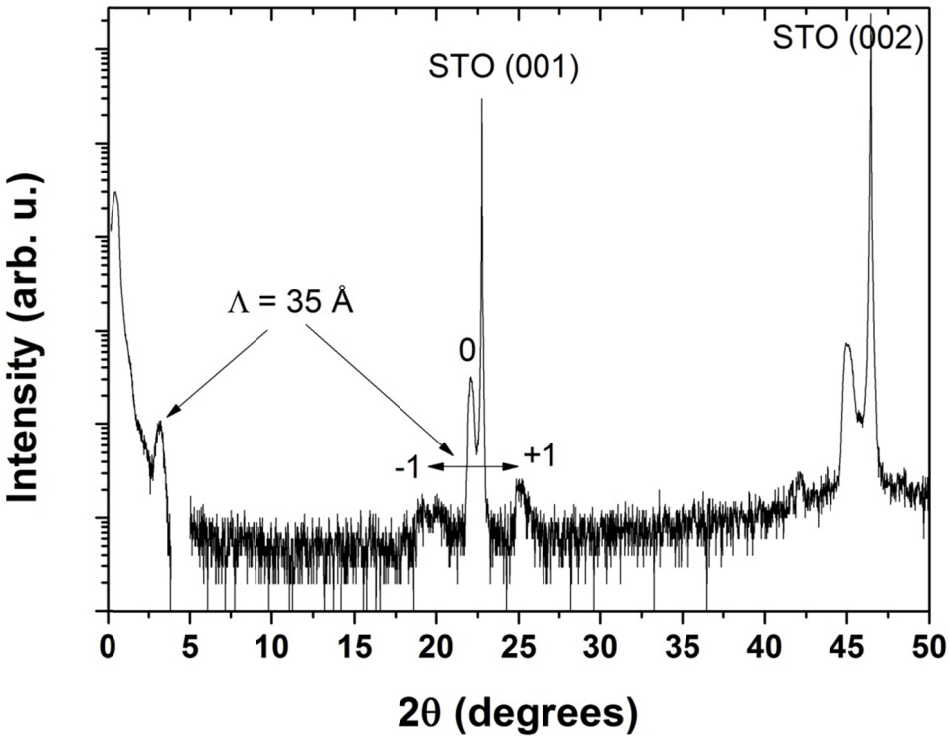

Figure S7. Out-of-plane θ-2θ X-ray Diffraction pattern for a $[(LaFeO_3)_5(YFeO_3)_5]_{40}$ grown on $SrTiO_3$ showing a Bragg peak at low angle consistent with a $10a_p$ ordering and weak satellite reflections around the main diffraction peak. The splitting of the peaks indicates the presence of different domains due to the difference of the out of plane lattice parameters.

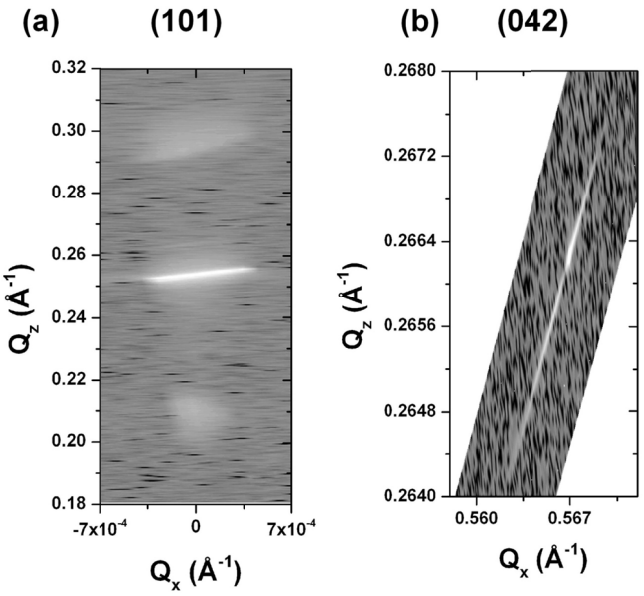

Figure S8. Reciprocal space maps of a $[(YFeO_3)_5(LaFeO_3)_5]_{40}$ heterostructure measured around (a) the $(101)_{Pmna}$ out-of-plane diffraction peak showing the good coherence between the heterostructure satellite and the substrate and (b) on the $(042)_{Pnma}$ subcell reflection showing both the substrate and the film peaks

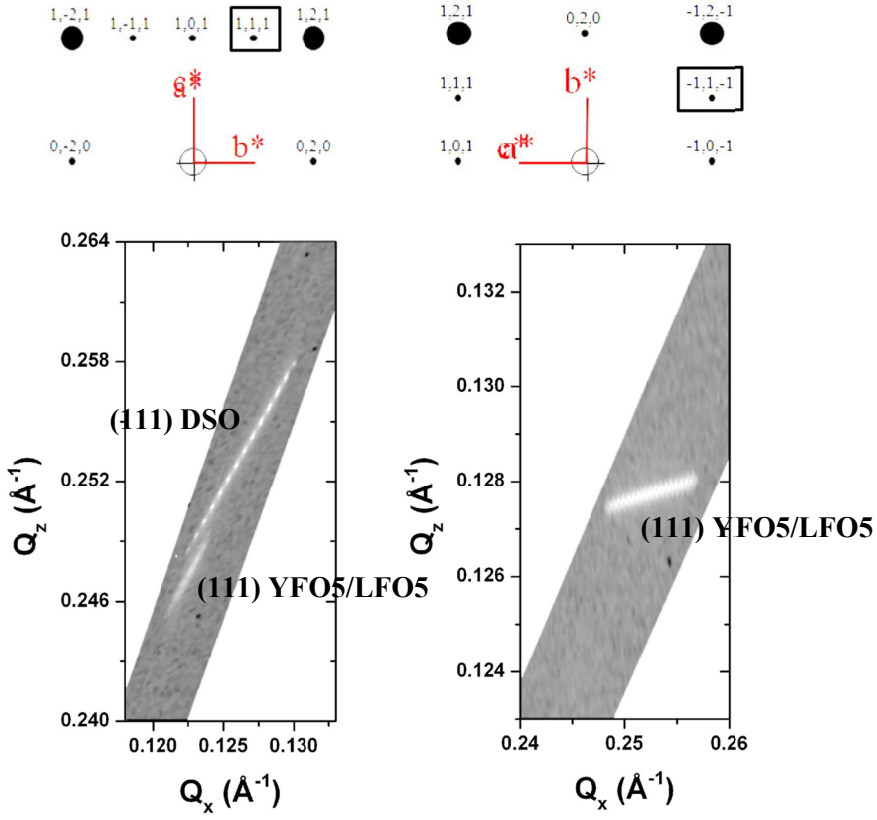

Figure S9. Reciprocal space maps of a $[(YFeO_3)_5(LaFeO_3)_5]_{40}$ heterostructure measured around the $(111)_{Pnma}$ subcell for (left) the non polar phase (χ=27°) where both substrate and film peaks are observed and (right) the polar phase (χ=63°)where only the film peak is observed. The simulated reciprocal space for each domain is shown on top with a black square showing which region is scanned.

4 Magnetic properties

4.1 SQUID Magnetometry

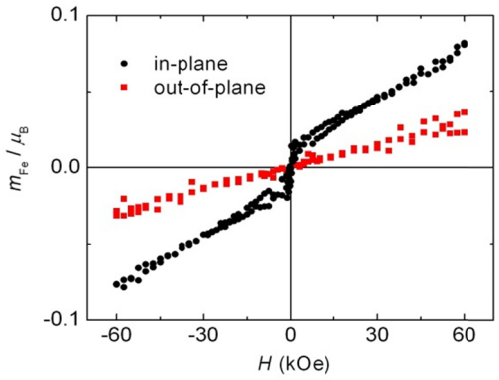

Figure S10. Magnetization hysteresis loops measured at T=300K on $[YFO_5/LFO_5]_{40}$ on STO (001) in magnetic field applied parallel (in-plane) and perpendicular (out-of-plane) to the film surface using a SQUID magnetometer.

Sample data have been corrected for the diamagnetic susceptibility of $SrTiO_3$ (100) substrates, measured at 300 K. Ferromagnetic contamination was removed by annealing the substrates used at 650 K in air for 2h as described by Yee *et al.*[1]

4.2 Magneto-optical Kerr Effect (MOKE)

Magneto-optical effects originate from magnetic perturbations of the dielectric permittivity tensor, where MOKE describes a change in the polarization of the reflected light, being linear proportional to the magnetization of the reflecting surface. MOKE has been extensively studied in orthoferrite materials[2]. Based on those studies a laser light source with the photon energy 3.0 eV was used, which activates the charge-transfer transition $t_{2u}^{n}(\pi)$--> t_{2g}* in Fe^{3+} ions in octahedral crystal field of O^{2-} ligands, thus producing one of the strongest maxima in the magneto-optic spectrum.

The longitudinal geometry (magnetic field applied parallel to both the film surface and to the plane of incidence) is primarily used to measure the magnetization components along the magnetic field, that is, in the film plane. However, the same geometry is also sensitive to the out-of-plane magnetization component if it does exist, as shown by numerical analysis of a similar MOKE setup.[3] The corresponding Kerr-rotation $\phi \propto a_1 m_x - a_2 m_z$, where a_1 and a_2 are parameters depending on material constants and angle of incidence. m_x and m_z denote the in-plane magnetization component along the applied field and the out-of-plane magnetization component, respectively.

Because of the anisotropic orbital angular momentum quenching[2] the corresponding off-diagonal elements of the dielectric permittivity tensor, ε_{ij}, are proportional not only to the uncompensated magnetization, **m**, as usual, but also to the transverse antiferromagnetic (AF) vector **l**,[4]

$$\varepsilon_{ac}=-\varepsilon_{ca}=i(\alpha_1 m_b+\beta_1 l_a) \quad \text{(S1)}$$

$$\varepsilon_{bc}=-\varepsilon_{cb}=i(\alpha_2 m_a+\beta_2 l_b) \quad \text{(S2)}$$

where α_1, α_2, β_1 and β_2 are coefficients, and ***m*** and ***l*** are uncompensated magnetization and AF vector projections along the corresponding orthorhombic unit cell axis. Note that since the weak ferromagnetic (WFM) magnetization ***m*** is generated by AF spin canting, increasing the absolute value of ***m*** in the applied magnetic field would correspond to decreasing the AF vector projection ***l*** perpendicular to the field, and vice versa.

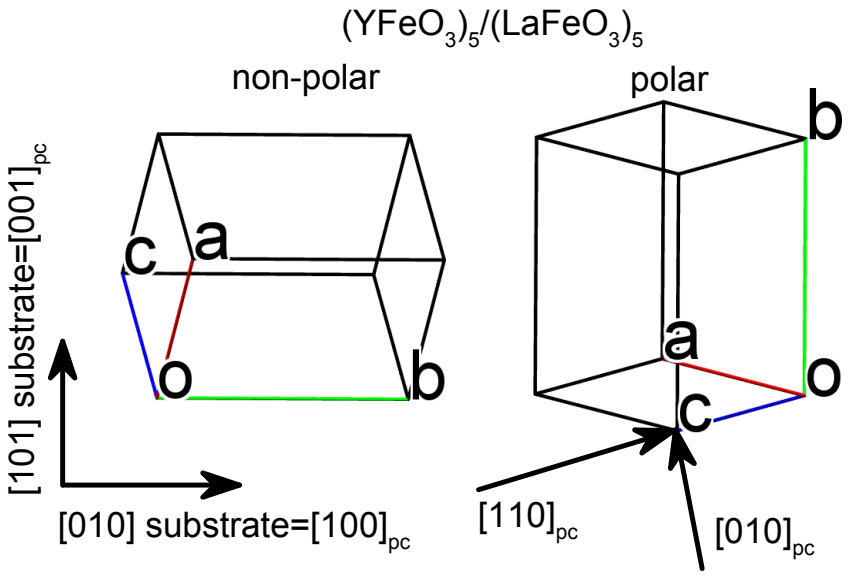

Figure S11: Three-dimensional drawings of orthorhombic unit cells corresponding to the polar and non-polar phases in $(YFeO_3)_5/(LaFeO_3)_5$ and their orientations with respect to orthorhombic (Pnma) or pseudo-cubic (pc) crystal axis of $(101)_{Pnma}$ substrate.

$(101)_{Pnma}$ $DyScO_3$		$(101)_{Pnma}$ non-polar $(YFeO_3)_5/(LaFeO_3)_5$	$(010)_{Pnma}$ polar $(YFeO_3)_5/(LaFeO_3)_5$
pseudo-cubic (pc)	Pnma	Pnma	Pnma
[1 0 0]	[0 1 0]	[0 1 0] m_{WFM} in Γ_4	[1 0 1]
[1 1 0]	[1 1 $\overline{\mathbf{1}}$]	[1 1 $\overline{\mathbf{1}}$]	[1 0 0] m_{WFM} in Γ_2
[0 1 0]	[1 0 $\overline{\mathbf{1}}$]	[1 0 $\overline{\mathbf{1}}$]	[1 0 $\overline{\mathbf{1}}$]
[0 0 1]	[1 0 1]	[1 0 1]	[0 1 0] m_{WFM} in Γ_4
[0 1 1]	[1 0 0]	[1 0 0] m_{WFM} in Γ_2	[1 1 $\overline{\mathbf{1}}$]

The expected MOKE responses depending on the magnetic structure (Γ_2 or Γ_4):

Non-polar phase (grown with the long axis b along [010] direction of the DSO (101) substrate):

If the magnetic field is applied along $[010]=[100]_{pc}$ of the DSO substrate, in orthorhombic and pseudo-cubic notation, respectively: the MOKE signal should contain WFM hysteresis if the Γ_4 magnetic structure where the WFM moment lies along the b axis is adopted (compare Fig. 10a and 10b). When the magnetic field is along $[110]_{pc}$ of the DSO substrate, then the WFM moment is oriented at an angle of 45 degrees to the magnetic field, that is, a hysteresis is possible, since the field projection along the easy WFM axis $[010]_{Pnma}$ is still about 70% of the applied field (compare Fig. 10a and 10b, for magnetic data on single crystal of $YFeO_3$[5]. If the magnetic field is applied along $[010]_{pc}$ of the DSO substrate, then the WFM moment is perpendicular to the field, and no hysteresis is expected. Since the transverse AF vector component would be zero, too, no contribution to the MOKE signal would be expected according to Eq. (S1) (compare Fig. 10a and 10b). Analog, under assumption of the Γ_2 magnetic structure one would expect a WFM hysteresis loop if the field is applied along $[010]_{pc}$ and no loop if the field is along $[100]_{pc}$. This is the opposite to the observed results (Fig. 10a). Based on the results shown in Fig. 10a, the magnetic configuration for the non-polar phase is Γ_4.

B: **Polar phase** (with the long axis b growing along [101] of the substrate):

If the magnetic configuration is Γ_4, then under all in-plane orientations of the magnetic field, the WFM moment should be oriented perpendicular to the field (out-of-plane), therefore no WFM hysteresis is expected. If the magnetic configuration of the polar phase is the alternative one, that is Γ_2, the WFM magnetization should be in-plane and emerge in form of a WFM hysteresis loop in case the field is applied along or at least at an angle of 45 degrees to the easy axis a (=along $[110]_{pc}$ of the substrate, see Fig. S11 and the table below. Since no WFM hysteresis loop is observed in the latter case (Fig. 10a), when the field is applied along $[010]_{pc}$, the configuration Γ_2 is improbable. In the case of the Γ_4 configuration the hard axis (out-of-plane) magnetization as well as the corresponding transverse AF vector could still contribute to the total MOKE signal, however with the opposite sign if compared to the in-plane contribution. This explains the negative slope of the hysteresis loops shown for $[(YFeO_3)_5/(LaFeO_3)_5]_{40}$ and $LaFeO_3$ thin films grown on DSO presented in Fig. 10. The degree of the negative slope is likely to be proportional to the number of structural domains grown with the b-axis out-of-plane (=polar phase in the case of $(YFeO_3)_5/(LaFeO_3)_5$, see Fig. 10d). The experimental results shown in Fig. 10a are in agreement with the polar phase adopting magnetic configuration Γ_4. $(YFeO_3)_5/(LaFeO_3)_5$ heterostructures demonstrated (Fig. 10a) sharp hysteresis loops, similar to those observed on $LaFeO_3$ thin films (Fig. 10c). In comparison to those cases the $YFeO_3$ films showed similar magnetic anisotropy (Fig. 10b) but elongated hysteresis loops, which could be explained by the higher number of structural defects in those films due to the higher amount of the growth strain (-3.3%), that is, higher mismatch to $DyScO_3$ substrate, if compared to $LaFeO_3$ (mismatch -0.3%)and $(YFeO_3)_5/(LaFeO_3)_5$ (mismatch +0.1% and -0.2% for non-polar and polar phases, respectively).

Both systems, YFeO3 and $LaFeO_3$ films on $DyScO_3$ and $(YFeO_3)_5/(LaFeO_3)_5$ on $SrTiO_3$ showed similar coercive fields of about 1kOe, in agreement with the literature values[5] for in-plane magnetization in YFO films on STO substrates. In comparison to those, broader loops in the case of YFO-LFO films grown on DSO substrates with coercivity fields of about 5kOe could be related to the interfacial distortion in the polar phase.

5. Second Harmonic Generation

Polar SHG dependences measured by polarizer rotation (angle θ) with fixed sample position:

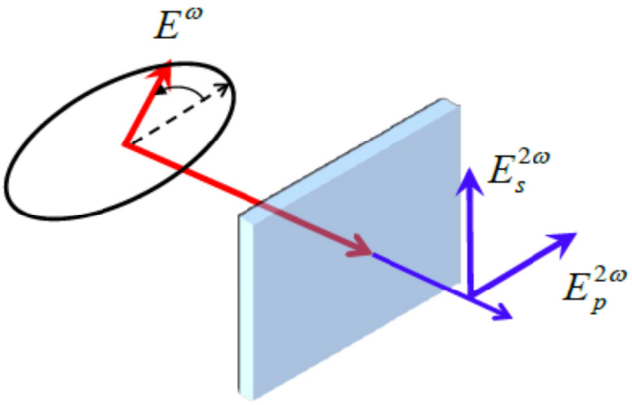

Figure S12. Schematic representing the geometry in which the rotational SHG dependence is measured with polarizer rotation (with the sample fixed) presented in the main text

The SHG intensity vs. θ curves in Fig. 12 were fitted using the following equation

$$I^{2\omega} = C_0 + C_2 \cos 2\theta + C_4 \cos 4\theta + S_2 \sin 2\theta + S_4 \cos 4\theta \qquad \text{(S3)}$$

6. Electrical characterisation

The in-plane conductivity of the film was measured in a two probe configuration at room temperature using a electrometer (Keithley model 6430). The contacts were made using gold wires and indium solder. The conductivity was found to be 4.10^{-7} S/cm, the sample is therefore considered insulating at room temperature, a requirement to perform dielectric measurement.

7. PFM details

The piezoelectric properties of the samples were characterized using a modified piezoelectric force microscopy (PFM) technique. PFM is based on the standard contact mode atomic force microscopy (AFM) setup with the cantilever and tip being electrically conductive[6]. For piezoelectric samples a voltage applied between the tip and a bottom or surface electrode results in sample strains due to the inverse piezoelectric effect[7]. The sample strains cause vertical and lateral deflection of the cantilever which can be accurately measured using appropriate calibration methods. In order to separate the topography and piezoresponse signals and also to increase the signal to noise ratio a lock-in amplifier technique is used, with the voltage applied to the tip having a much larger frequency compared to the scanning frequency.

The profiles were measured with the cantilever parallel to the electrodes (Fig.S13) using lock-in amplifiers at 10 kHz with amplitude of 1 V. Various voltage offsets were used as indicated in Figure 5 d. The measurement frequency was chosen away from any cantilever resonance. The strain in the thin film underneath the electrodes is driven by the active regions between electrodes, resulting in a spatially alternating stretching/compression about their centre. At the same time, the thin film is displaced vertically, again alternating in sign between adjacent electrodes. By changing the voltage offset used, both the displacement amplitudes and signs can be changed. This is due to the electric field dependence of the piezoelectric coefficients[7]. As we have verified in Figure S13 (c) the displacement amplitudes change linearly with voltage offset, showing a non-hysteretic behaviour with coercive voltage of 2 V.

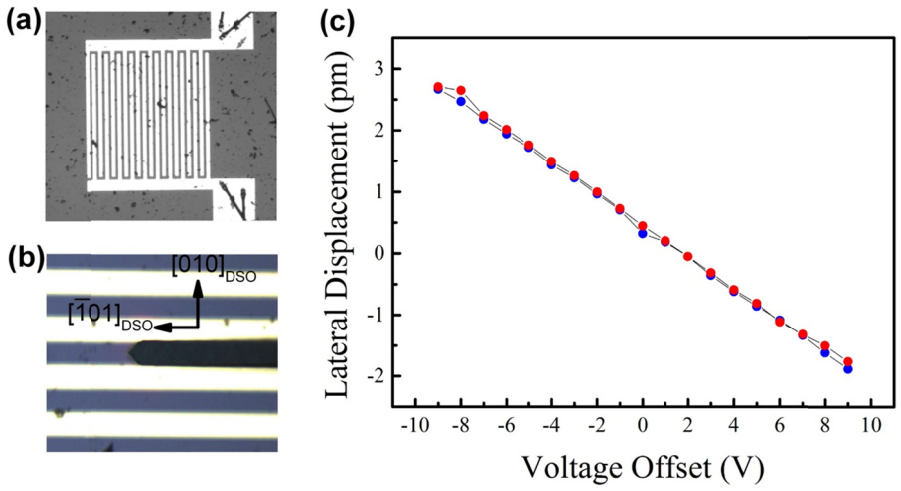

Figure S13. (a) Optical microscope images of the interdigital electrodes on top of the film (b) Respective orientation between the electrode and the *Pnma* axes of the $DyScO_3$ substrate (DSO). (c) Variation of the displacement amplitude as a function of the voltage offset.

The response of piezoelectric materials to electric fields and stresses is described by the system of strain-charge equations[7],

$$S = s^{Ec}T + d^{T}E$$
$$D = dT + \varepsilon^{Tc}E \qquad \text{(S4)}$$

where T and E are the stress and electric field vectors, respectively, S and D are the strain and electric displacement field vectors, respectively. s^{Ec} denotes the compliance tensor for constant electric field, d is the piezoelectric tensor and ε^{Tc} is the permittivity tensor under constant stress. The piezoelectric tensor depends on the crystal structure and orientation, and thus also on the direction of the electric polarization. In order to verify the piezoelectric nature of the response shown in Figure 13 in the main text and the electric polarization direction, finite element simulations based on Equation 8 were performed for the measured sample geometry. The DSO substrate was modelled as a linear elastic material using literature values[8]. The back of the substrate was fully fixed in the simulations - in experiments the substrate was rigidly glued onto a metal plate. Moreover due to the interdigitated electrode structure long-range substrate deformations are negligible. The thin film heterostructure was modelled as a piezoelectric material, 160 nm thick, with a given polarization direction. Based on density functional theory calculation for the measured material we obtain the piezoelectric tensor

$$d/(pC/N) = \begin{bmatrix} 0 & 0 & 0 & -1.4 & 0 & 0 \\ 0 & 0 & 0 & 0 & 0.5 & 0 \\ -2.8 & -4.2 & 6.1 & 0 & 0 & 0 \end{bmatrix}$$

For the simulations, the polarization direction, and thus the piezoelectric tensor, is rotated to lie along a given direction, and the displacement profile was calculated for a potential of 1 V applied to a series of interdigitated electrodes, as in the measurements. The elastic properties of the thin film heterostructure depend on Young's modulus, Y, and Poisson's ratio, ν, of the material. The best

agreement between the simulations and the experimental data can be achieved by varying the ratio v/Y.[12] Within the order of magnitude, a good match between experiment and simulation is obtained for $v/Y = 10^{-12}$ (m^2/N) and electric polarization perpendicular to the electrodes. This corresponds to the [-101] direction in the *Pnma* subcell coordinate system.

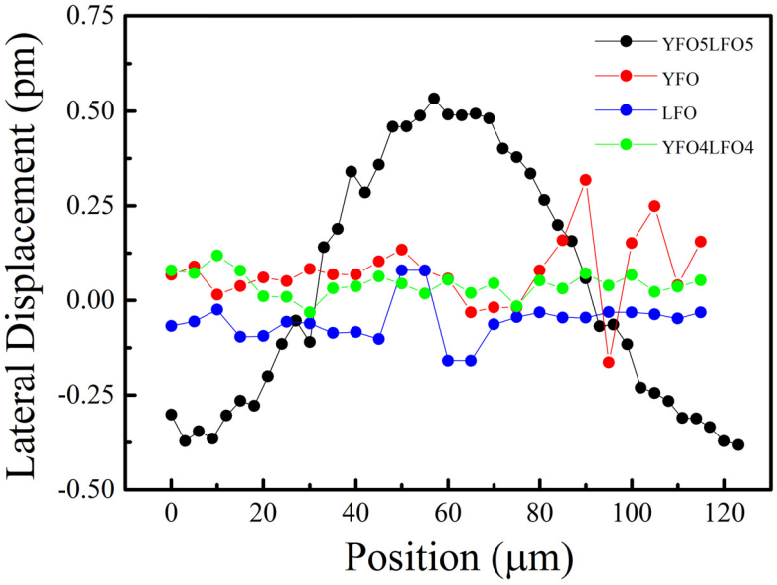

Figure S14. Lateral piezoresponse profile measurement on single layer of $YFeO_3$ (red), $LaFeO_3$ (blue) and $[(YFeO_3)_4(LaFeO_3)_4]_{50}$ grown on DSO (101) in the same condition as the heterostructure showing no piezoelectric effect within the limit of detection of the setup.

(1) Yee, S. M. M.; Crandles, D. A.; Gonchrova, L. V. *J. Appl. Phys.* **2011**, *110*, 033906.
(2) Kahn, F. J.; Pershan, P. S.; Remeika, J. P. *Phys. Rev.* **1969**, 3.
(3) Vavassori, P. *Appl. Phys. Lett.* **2000**, *77*, 1605.
(4) Krichevstov, B. B.; Pisarev, R. V.; M., R. M. *Sov. Phys. Solid State* **1980**, *22*, 1240.
(5) Scola, J.; Noun, W.; Popova, E.; Fouchet, A.; Dumont, Y.; Keller, N.; Lejay, P.; Sheikin, I.; Demuer, A.; Pautrat, A. *Phys. Rev. B* **2010**, *81*, 174409.
(6) Kalinin, S.; Gruverman, A. *Scanning Probe Microscopy: Electrical and Electromechanical Phenomena at the Nanoscale*; Springer, 2007.
(7) Damjanovic, D. *Rep. Prog. Phys* **1996**, *61*, 1267.
(8) Janovská, M.; Sedlák, P.; Seiner, H.; Landa, M.; Marton, P.; Ondrejkovič, P.; Hlinka, J. *J. Phys. Cond Mat.* **2012**, *24*, 385404.